Consolidation of bone-like apatite bioceramics by spark plasma sintering of amorphous carbonated calcium phosphate at very low temperature

C. Ortali, I. Julien, M. Vandenhende, C. Drouet, Eric Champion

Original Article

Consolidation of bone-like apatite bioceramics by spark plasma sintering of amorphous carbonated calcium phosphate at very low temperature

C. Ortali[a], I. Julien[a], M. Vandenhende[a], C. Drouet[b], E. Champion[a,*]

[a] Univ. Limoges, CNRS, SPCTS, UMR 7315, F-87000 Limoges, France
[b] CIRIMAT, Université de Toulouse, CNRS, INPT, UPS, ENSIACET, 31030 Toulouse, France

ARTICLE INFO

Keywords:
Bioceramic
Carbonated apatite
Spark plasma sintering
FTIR analysis
Bone substitute

ABSTRACT

Various carbonated calcium phosphate powders were synthesized by aqueous precipitation and ceramics consolidation by spark plasma sintering (SPS) at very low temperature was investigated. The objective was to preserve low crystallinity and avoid material decarbonation. SPS at low temperature only leads to little or no sintering when crystallized powders are used. Amorphous powders are required. In this case, consolidation occurs at temperatures below 150 °C. It is accompanied by crystallization of the amorphous phase into calcium-deficient carbonated apatite $Ca_{10-x-y}(PO_4)_{6-x-y}(HPO_4)_x(CO_3)_y(OH)_{2-x-y-2z}(CO_3)_z$. The resulting ceramics are microporous and highly cohesive with good mechanical properties (flexural strength = 18 MPa). The sintering mechanism, called "crystal fusion", is based on solid state diffusion of chemical species at the grain boundary and crystal growth within the amorphous particles. These bioceramics that mimic the composition of the bone mineral are expected to have a higher bioreactivity than well crystallized carbonated hydroxyapatite ceramics obtained by conventional sintering.

1. Introduction

Synthetic hydroxyapatite (HA) of chemical formula $Ca_{10}(PO_4)_6(OH)_2$ is commonly used as bone substitute due to excellent biocompatibility and osteoconductive properties [1,2]. Calcium phosphate apatite can accept multiple ionic substitutions as well as vacancies in its crystal lattice [3,4]. Thus, the mineral part of bone is composed of a low crystalline and poly substituted nonstoichiometric apatite [5]. Carbonate (CO_3^{2-}) is the main substituted ionic group in biological apatites, with amounts ranging from 3 to 8 wt% [6,7]. A mean chemical formula of bone mineral apatite was proposed by Legros et al. as follows: $Ca_{8.3}(PO_4)_{4.3}(CO_3,HPO_4)_{1.7}(CO_3,OH)_{0.3}$ [5]. As shown in this formula, carbonate ions can be incorporated in the apatite lattice in replacement of hydroxide ions (OH^-), named "A type substitution" (referred as C_A in the text), leading to the formula $Ca_{10}(PO_4)_6(OH)_{2-2y}(CO_3)_y$ with $0 \leq y \leq 1$. Synthetic A type carbonated HA (C_AHA) can be produced by calcination of a stoichiometric HA powder under dry CO_2 flux at 900 °C for several hours according Trombe's method [8–10]. Carbonate can also substitute for phosphate ions (PO_4^{3-}), named "B type substitution" (referred as C_B in the text) leading to the formula $Ca_{10-x}(PO_4)_{6-x}(CO_3)_x(OH)_{2-x}$ with $0 \leq x \leq 2$. Synthetic B type carbonated HA (C_BHA) can be obtained by aqueous precipitation [11–14]. Additionally, mixed AB type carbonated HA ($C_{AB}HA$, $Ca_{10-x}(PO_4)_{6-x}(CO_3)_x(OH)_{2-x-2y}(CO_3)_y$) can be produced by heating a C_BHA under controlled atmosphere containing CO_2 and water vapor partial pressures [14]. Due to these substitutions, such carbonated apatites are expected to exhibit better biological properties in terms of resorbability than pure HA [15–18]. We have shown recently that mixed $C_{AB}HA$ ceramics containing carbonates in similar amount to that found in the natural bone, exhibited enhanced biodegradability associated to an optimal balance for osteoblast and osteoclast activity (i.e. the main cells involved in bone regeneration) [19].

However, a serious drawback of carbonate apatites is their thermal instability. This material decomposes by decarbonation at "low" temperature (from about 450 °C under air atmosphere) which makes the consolidation of ceramic parts difficult by conventional natural sintering [20–23]. Consequently, these ceramics are sintered between 800 °C and 1000 °C under a flow of CO_2 gas (wet or dry according to the desired substitutions) to prevent the decarbonation reaction to occur, preserve carbonate groups located in B sites of the structure and avoid the formation of secondary phases such as lime or calcite [14,23]. Another approach to avoid the decomposition of the material could be sintering faster and/or at lower temperature using a non conventional sintering method such as Spark Plasma Sintering (SPS).

SPS has been investigated since the 1990s for the flash sintering of several ceramic materials. Its principle is based on a pulsed current

* Corresponding author at: Centre Européen de la Céramique, SPCTS, UMR CNRS 7315, 12, rue Atlantis, 87068 Limoges Cedex, France.
E-mail address: eric.champion@unilim.fr (E. Champion).

https://doi.org/10.1016/j.jeurceramsoc.2017.11.051

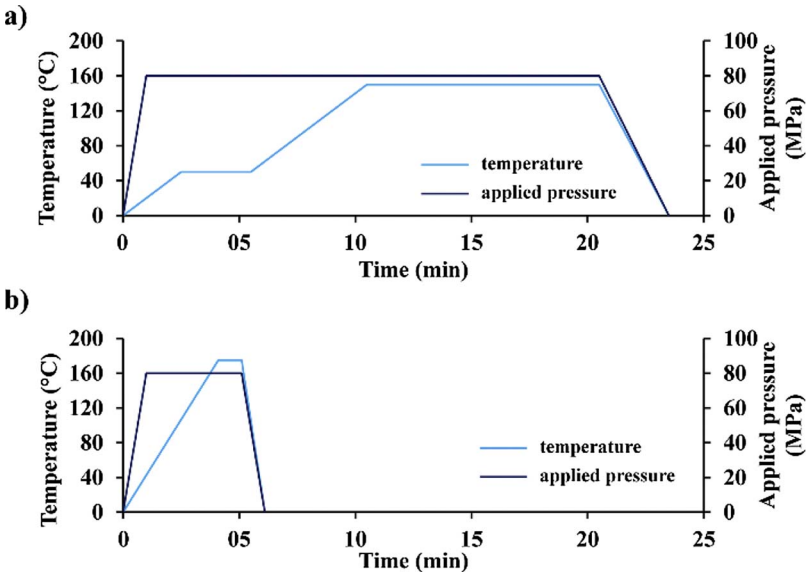

Fig. 1. SPS temperature and pressure programs a) influence of powder properties and b) influence of applied pressure (60–120 MPa).

passing through a conductive pressing die containing the sample, and consecutive heating by Joule effect, under compressive stress. This process is generally known to limit the grain growth and to lower the sintering temperature [24,25]. SPS of HA has been investigated by several research teams. The SPS temperature ranged from 900 °C to 1000 °C and led to high bulk density (> 99% of the maximum value) without the formation of any secondary phase. This increased the strength of the ceramic and limited grain growth [26 28].

Low crystallinity and nonstoichiometry, as in natural bone apatite, are other key factors to improve the biodegradability of apatitic synthetic materials. With this aim, synthetic nanocrystalline apatites were investigated. It was shown that these materials exhibit low crystallinity with a non apatitic hydrated surface layer including ions such as CO_3^{2-}, HPO_4^{2-}, Ca^{2+} or OH^- [29 32]. This layer is responsible for the high reactivity of nanocrystalline apatites in terms of biology (e.g. adhesion of proteins) [31] and chemistry due to high mobility of non apatitic ionic species (allowing easy ion exchanges with the surrounding environment) [33]. Nevertheless, the production of cohesive ceramic parts is a difficulty since high temperature treatment would lead to thermal decomposition and eliminate the hydrated non apatitic surface layer of particles. In order to preserve such features previous studies explored SPS of non carbonated nanocrystalline apatites at low temperature (typically lower than 300 °C) [34 36]. Recently, this method has also been investigated to consolidate iodate substituted hydroxyapatite for nuclear application in the conditioning of radioactive iodine 129 [37].

From this context, and in order to further increase the resorbability of apatitic compounds by incorporation of carbonate ions in the lattice, the objective of this work was to investigate the processing ability of low crystalline carbonated apatite ceramics. With this aim, powders having various chemical compositions (i.e. carbonate contents) and crystallinity degrees were prepared by aqueous precipitation. Then, SPS of these powders at very low temperature (150 °C) was performed. The structure, chemical composition and mechanical resistance of the processed ceramics were then investigated.

2. Experimental

2.1. Synthesis of carbonated phosphocalcic powders

Powders were prepared by precipitation in aqueous medium according to a protocol described previously [14]. Briefly, a solution of diammonium hydrogen phosphate ($(NH_4)_2HPO_4$, 98.7%, Fisher Chemical) and ammonium hydrogencarbonate (NH_4HCO_3, > 99.0%, Sigma Aldrich) is added to a calcium nitrate solution ($Ca(NO_3)_2{,}4H_2O$, 99%, Sigma Aldrich) at constant pH and temperature. The C/P ratio, designating the molar ratio in which the phosphate and carbonate ions were introduced, was set at 0.125. The amount of reagents was also fixed in order to have a Ca/P molar ratio equal to 1.667. The pH was maintained at a value of 9 by addition of an ammonium hydroxide solution (NH_4OH 35%, Fisher Chemical). Three synthesis temperatures were investigated: 90 °C, which was close to the boiling point of the solution, 60 °C as an intermediate temperature and 37 °C the physiological temperature of the human body. The synthesis reactor was put under argon flow. When the last drop of phosphate and carbonate solution was added, the mixture was left to mature for 30 min. After this maturation, the precipitate was filtered on a Buchner funnel, then washed with 250 mL of distilled water per gram of powder and finally lyophilized.

2.2. Spark plasma sintering

Sintering of ceramic pellets was performed using a SPS Dr.Sinter 825 from Fuji Electronic Industrial Company (Japan). It involves application of a uniaxial compressive load on the sample and simultaneous heating by a pulsed continuous electrical current.

The sintering behavior of powders synthesized at different temperatures (37 °C, 60 °C and 90 °C) was studied. Weighed 300 mg of powder was introduced into a 10 mm diameter graphite die previously covered with Papyex®, a thin graphite foil, to facilitate the demolding of the sample after SPS. Fig. 1a gives the SPS temperature and pressure cycles used in this study. The sintering temperature was set at 150 °C with a heating rate of 20 °C min^{-1}. The pressure was set to 80 MPa, applied in 1 min. After application of the compressive stress a dwell was made at 50 °C during a few minutes to homogenize the temperature in the enclosure of the SPS device. Each test was carried out under argon atmosphere.

Influence of the applied pressure (60 MPa, 80 MPa, 100 MPa and 120 MPa) was also investigated. For this study, the SPS cycle was modified (Fig. 1b): whatever the final pressure, the load was applied within 1 min. The final temperature was set at 175 °C for a short dwell (1 min) with a 40 °C min^{-1} heating rate and without dwell at 50 °C. Pressureless SPS was also performed. The powder was initially compacted under a 80 MPa compressive pressure applied for 1 min before heating. Then, the mechanical pressure was removed and the thermal cycle described in Fig. 1a was applied.

The in situ densification curves were registered from the measure ment of the moving piston displacement and the temperature measured by a thermocouple placed close to the sample inside a hole drilled in the graphite die. The relative density (or densification ratio) of SPS samples corresponded to the ratio between the apparent density, determined by Archimedes' method in water, and the real solid density, obtained by helium pycnometry measurements (Micromeritics, AccuPyc II 1340).

Complementary hot pressing (HP) experiment was performed in a Goliath LPA (2000 °C, 5 tons), ECM Technologies (Applied Physics). The same protocol of sample preparation as that described for SPS was used. The temperature was measured on the external wall of the gra phite die containing the sample. The dwell temperature was set at 400 °C for 10 min with a heating ramp of 15 °C min^{-1}. A 80 MPa compressive stress was applied at the beginning of the heating cycle. At the end of dwell at 400 °C, the temperature and the load were decreased gradually. The displacement of the piston applying the mechanical load was measured during the test.

2.3. Samples characterization

X ray diffraction patterns of precipitated powders and SPS ceramics were acquired on a BRUKER D8 Advance diffractometer using the CuKα radiation. The patterns were recorded in a 2θ range 20° − 60° with a step size of 0.02° and a dwell time of 0.51 s. Phase identification was performed by comparing the experimental diagram with the database of diffraction patterns (PDF) of the International Center for Diffraction Data (ICDD). Lattice parameters were refined by profile fitting using the JANA2006 software (Czech Republic). Diffraction peaks were fitted according to a pseudo Voigt function, allowing the system to be ani sotropic. The crystallite size L_{hkl} was determined from two peaks ((002) and (310) giving respectively the mean crystallite length and width) by the Scherer Eq. (1) [38] and using the Peakoc software (France):

$$L_{hkl} = \frac{\lambda}{\cos\theta_{hkl}\sqrt{\beta_{exp}^2 - \beta_0^2}} \quad (1)$$

with λ, the radiation wavelength; β, the full width at half maximum of the peak and θ, the diffraction angle of the associated (*hkl*) plane. The lattice distortion parameter g_{hkl} in the crystallographic direction (00*l*) was also calculated based on the model of Hoseman and Vogel (Eq. (2)) [39]:

$$\sqrt{\beta_{exp}^2 - \beta_0^2} = \frac{1}{L_{hkl}} + \pi^2 \frac{g_{hkl}^2}{d_{hkl}} m^2 \quad (2)$$

with *m* the reflexion order and d_{hkl} the reticular distance of (*hkl*) planes family, applied here to the family of planes (00*l*).

Temperature programmed X Ray diffraction was performed using the same diffractometer, in an ANTON PAAR, NTK 1200N oven. Powder was placed in an alumina crucible lined with platinum foil. The maximum temperature was set at 1000 °C with a heating rate of 10 °C min^{-1} under nitrogen flow. The patterns were acquired in the 2θ range 27 38° with a step size of 0.02° and a dwell time of 1.0 s, every 20 °C during a temperature plateau of 11 min.

Infrared spectra were collected on a NICOLET 5700 spectrometer. The spectra were recorded in transmission mode, using KBr pellets, over the 4000 400 cm^{-1} range with a resolution of 2 cm^{-1} from an accu mulation of 64 scans.

For quantitative chemical analysis, calcium and phosphorus con tents were determined by Inductively Coupled Plasma/Optical Emission Spectroscopy (ICP/OES) on a PERKIN ELMER, Optima 8300, Optical Emission Spectrometer. The analysis was performed in solution from about 30 mg of powder dissolved in perchloric acid prepared at 6 mol L^{-1} (70%, AnalaR NORMAPUR) and diluted in 100 mL of water. Carbonate content of powders was determined by elemental analysis (HORIBA, Carbon analyzer, EMIA 321V) consisting of burning 500 mg of powder sample placed in a crucible with a metallic blend (iron, copper, tin) in order to initiate the combustion. Carbonate content of apatite powders and sintered ceramics was also evaluated using FTIR spectroscopy according to Grunenwald et al. method [40]. FTIR was also used to estimate the proportions of carbonates within the various chemical sites (i.e. A or B type or labile, the latter corresponding to carbonates in non crystallized environment).

The morphology of powders and the microstructure of SPS ceramics were observed by scanning electron microscopy operating in secondary electron mode (JEOL, FEG SEM, JSM 7400F) and transmission electron microscopy (JEOL HR TEM 2100). TEM also allowed to record selected area electron diffraction (SAED) patterns. For powders, some grains were dispersed in acetone and placed on a steel sample holder prior to SEM examination and on a mesh Cu grid with a carbon membrane for TEM. The pellets observed by SEM were fixed on the sample holder with adhesive carbon tape.

Biaxial flexural strength was measured on 10 cylindrical samples obtained after SPS at 150 °C in a 30 mm diameter die and the strength value was calculated according to Meganck et al. method [41].

Specific surface area (S_{BET}) and bulk density (*d*) of powders were measured by the BET method (MICROMERITICS, ASAP 2020, 8 points) and by He pycnometer (MICROMERITICS, AccuPyc II 1340) respec tively. Differential Thermal Analysis (DTA) was conducted on 50 mg of powder using in a NETZSCH STA 449F3 equipment from 30 to 1200 °C with a heating rate of 10 °C min^{-1} under inert argon flow. Thermomechanical analysis (i.e. dilatometry) was realized on 3 mm thick pellet using the same thermal cycle as for DTA in a NETZSCH DIL402C device. The force applied by the probe was 25 cN. The sample was shaped by compaction of 300 mg of powder in a 10 mm diameter steel matrix under a pressure of 62.5 MPa.

3. Results and discussion

3.1. Powder synthesis and characterization

The XRD patterns of synthesized powders are presented in Fig. 2. Diffraction peaks corresponding to an apatitic phase (PDF 9 432) ap pear for the powders produced at 60 °C and 90 °C but with the lowering of the synthesis temperature, they become broader and poorly defined. The crystallite size (Table 1) is smaller for the powder synthesized at 60 °C than at 90 °C. In both cases the crystallites exhibit a preferred growth along the *c* axis of the apatite structure, the value of $L_{(310)}$ being about half the value of $L_{(002)}$. This anisotropic grain growth is typical of apatite crystals. Crystallinity is also related to lattice deformations, which can be evaluated using the lattice distortion parameter g_{hkl}. Its value is smaller for the powder prepared at 90 °C than at 60 °C (Table 1). Consequently, the powder synthesized at 90 °C shows less lattice distortions than the powder synthesized at 60 °C. This means

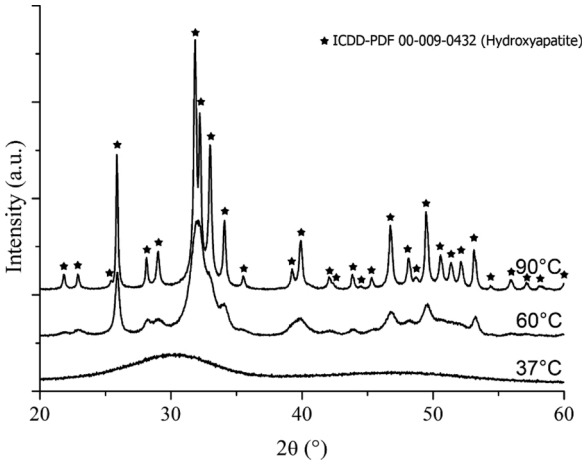

Fig. 2. XRD patterns of synthesized carbonated calcium phosphate powders.

Table 1
Powder crystallographic characteristics obtained by XRD peaks fitting.

Powder synthesis temperature	*60 °C*	*90 °C*
a lattice parameter (Å)	9.42(8)	9.42(4)
c lattice parameter (Å)	6.89(2)	6.90(1)
$L_{(310)}$ (Å)	78	257
$L_{(002)}$ (Å)	171	500
g_{hkl} (Å rad)	0.0101	0.0062

Table 2
Physical characteristics of synthesized powders.

$T_{synthesis}$	*37 °C*	*60 °C*	*90 °C*
S_{BET} (m^2 g^{-1})	45.8 ± 0.3	212.5 ± 0.5	68.0 ± 0.2
d (g cm^{-3})	2.515 ± 0.006	2.962 ± 0.003	2.938 ± 0.002

that, in agreement with literature data [11,21,22], the increase of the synthesis temperature increases the crystallinity of the powder (larger crystallite dimensions and lower distortion parameters). In comparison with the lattice parameters of stoichiometric HA (a = 9.418 Å and c = 6.884 Å according ICCD PDF file 00 009 0432) both *a* and *c* are greater for the two carbonated powders (Table 1). According to Legeros et al., the parameter *a* decreases when substituting carbonates in B site, these ions being smaller than phosphate ones. Landi et al. showed that the parameter *c* increases with this substitution [42,43]. In contrast, in the case of A type substitution, Elliot demonstrated that the value of *a* increases and *c* decreases [44]. In addition, contraction of the c axis and expansion in the perpendicular direction are generally observed for non stoichiometric apatites [45]. Consequently, additional substituted species (carbonates C_A and/or C_B, or HPO_4^{2-}) may have caused the enlargement of the crystallographic lattice in both directions *a* and *c*, which will be confirmed hereafter by the spectroscopic and chemical analyzes of these powders.

The XRD pattern of the powder synthesized at 37 °C, does not show any defined peak (Fig. 2), suggesting that the grains are amorphous. Only two broad and diffuse peaks with maxima at about 2θ ≈ 30° and 50° are registered which cannot be ascribed to an apatite feature. Moreover, this diffractogram is very similar to that of amorphous calcium phosphate (ACP) found in the literature data [46,47].

This also agrees with SEM and TEM observations (Fig. 3). The powder synthesized at 37 °C is made of agglomerated spherical grains which size varies from about 35 to 250 nm. Thus, in this powder grain growth during the synthesis process was isotropic, which was not the case of the crystallized powders. The amorphous character of this sample is also confirmed by the diffraction pattern produced by SAED. Here also, this powder presents the same morphological characteristics as ACP grains composed of so called Posner's clusters of composition close to ($Ca_9(PO_4)_6$,nH_2O) described in the literature [48,49]. Observations of the powder synthesized at 60 °C (Fig. 3) highlights nanometric needle like grains having an average size of about 40 nm length and 20 nm width. Due to its low crystallinity and very small grain size, this powder exhibits properties close to the nanocrystalline apatites described by Eichert et al. [31]. The powder synthesized at 90 °C is also made of rod shaped grains (Fig. 3), but of much larger size: about 150 nm length and 60 nm width. SAED patterns confirm that the grains precipitated at 60 °C and 90 °C are crystallized according to the apatite structure.

The bulk density *d* and the specific surface area S_{BET} of the powders are given in Table 2. The values of density measured for the crystallized powders (i.e., 2.96 and 2.94 g cm^{-3} after synthesis at 60 °C and 90 °C respectively) are not significantly different and close to that obtained by Lafon et al. (2.83 g cm^{-3} for a C_BHA precipitated at 90 °C in similar conditions) [14]. The density obtained for the amorphous powder synthesized at 37 °C is significantly lower than those of the crystallized powders. Its value (2.52 g cm^{-3}) approaches the bulk density calculated for ACP by Holt et al. at 2.31 g cm^{-3} [50].

The specific surface area of the raw powders is linked to the grain size observed by electronic microscopy. The amorphous calcium phosphate consisting of large spherical grains has the smallest specific surface area. The carbonated apatite powder synthesized at 90 °C, with the largest needle like grains has a greater surface area. It can be noted that the value obtained here is close to that of stoichiometric hydroxyapatite (68 m^2 g^{-1}) [51] but slightly higher than that found by Lafon et al. for carbonated apatite (36 m^2 g^{-1}) [14] synthesized in similar conditions. The powder synthesized at 60 °C has the largest surface area in accordance with its nanometric grain size.

FTIR spectra (Fig. 4a) were collected on the raw synthesized powders. For powders synthesized at 60 °C and 90 °C, typical vibration bands of phosphate groups in the apatite structure are observed at 472 cm^{-1} (ν_2) 560, 575 and 600 cm^{-1} (ν_4), 960 cm^{-1} (ν_1), 1020 1120 cm^{-1} (ν_3). The bands at 630 and 3560 cm^{-1} are assigned to apatitic OH groups [52,53].

Regarding the powder synthesized at 37 °C, the spectrum exhibits broad bands which are characteristic of a non crystalline material. These bands are similar to those found for ACP prepared by

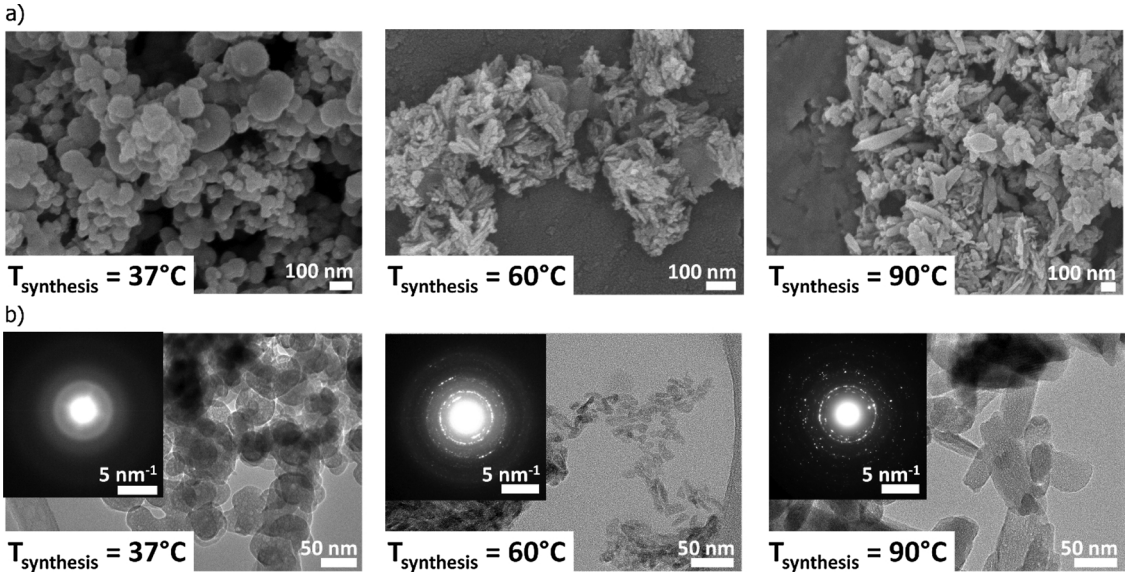

Fig. 3. Microscopic observations of powders synthesized at different temperatures: a) SEM, b) TEM and SAED patterns.

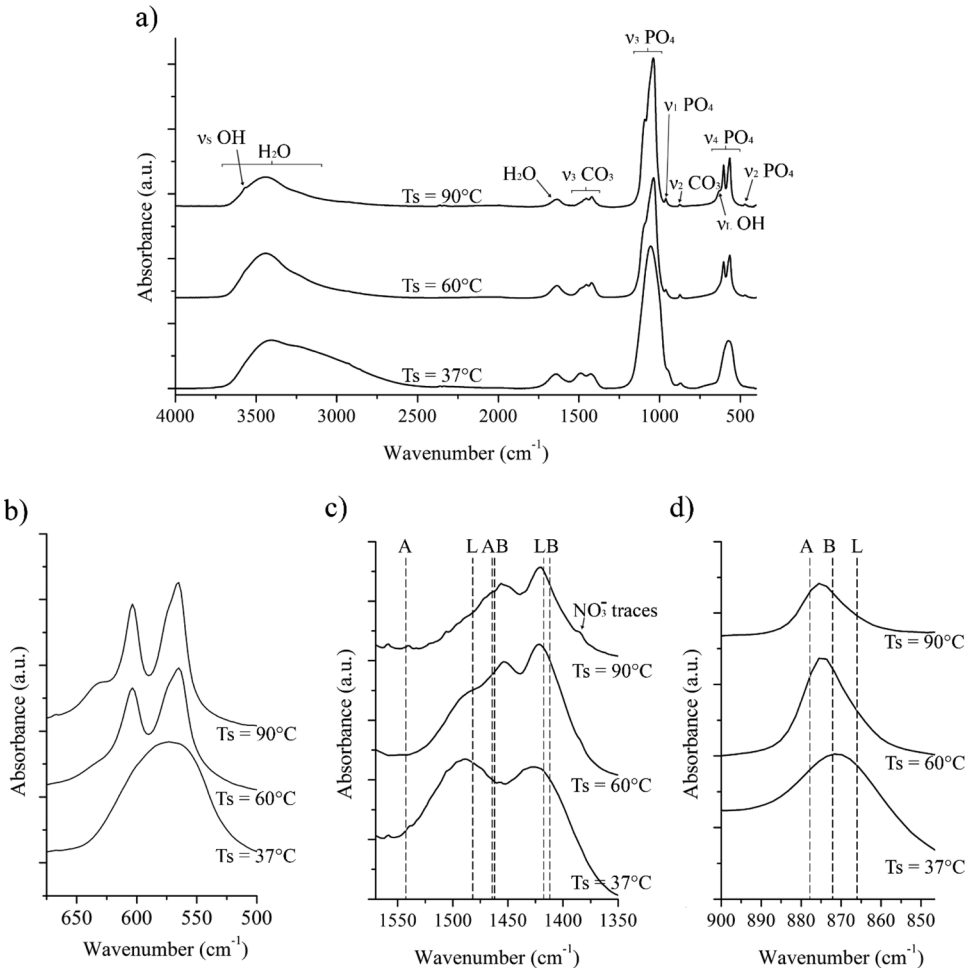

Fig. 4. FTIR spectra of synthesized powders: a) general spectra from 4000 to 400 cm ^{1}, b) zoom on the ν_4 PO_4 band, c) zoom on the ν_3 CO_3 band, d) zoom on the ν_2 CO_3 band. Contributions are denoted A for A-site, B for B-site and L for labile carbonate.

precipitation in an alkaline medium [53,54].

The amount of water, which can be estimated by the broad band between 3700 and 2800 cm^{-1} and the band at 1650 cm^{-1}, decreases with increasing the synthesis temperature. This water is mainly due to the presence of a hydrated layer at the surface of apatite nanocrystals as it was previously described for nanocrystalline apatites [31,45]. Water seems present in greater amount in the amorphous powder produced at 37 °C, which can be explained by the fact that constitution water can be found in the interstices between the amorphous clusters [48,50].

Carbonate ions can be observed in two regions of the spectra: the ν_2 vibrations of carbonate groups between 850 and 890 cm^{-1} and the ν_3 vibrations between 1400 and 1570 cm^{-1}. The ν_4 CO_3 band (in the range 760 665 cm^{-1}) [53] is too weak to be visible on the spectra and cannot be exploited. For each vibration mode, contributions can be attributed to the various environments of carbonate groups: A site, B site and labile carbonates. Table 3 gathers the characteristic wave numbers of these contributions based on literature reports.

Zooms of ν_2 and ν_3 CO_3 bands (Fig. 4*c* and *d*) focus on the main contributions of carbonate ions. For the powder synthesized at 90 °C, typical ν_3 bands of carbonates in B sites around 1412 cm^{-1} and 1462 cm^{-1} are observed. A shoulder is also observed around 1480 1500 cm^{-1} which could be attributed to labile carbonates. However, it could also be attributed to carbonates in A sites in mixed AB type apatites [55]. This hypothesis can be confirmed on the one hand by the presence of a very small peak at 1542 cm^{-1} attributed to A site carbonates and on the other hand by the examination of the asymmetrical ν_2 CO_3 band centered at 875 cm^{-1}, implying a major contribution of the B sites at 872 cm^{-1} with a minor A sites contribu tion at 878 cm^{-1}. Additionally, a light contribution of labile carbonates can be responsible for the enlargement of the band down to 860 cm^{-1}. Therefore, this powder contains predominantly B type carbonates but also minor A type and labile CO_3^{2-} species. The same conclusion can be drawn for the powder synthesized at 60 °C, but in this case a more important contribution of labile carbonates is observed, the shoulder at 1480 1500 cm^{-1} being characteristic of these labile carbonates. This was expected due to the less mature (less crystallized) character of the apatitic particles synthesized at lower temperature that include a non apatictic hydrated surface layer as described for other nanocrystalline apatites. The powder synthesized at 37 °C presents wide bands due to various ionic environments in the amorphous structure. Carbonates can be assimilated to labile surface carbonate species in immature nano crystalline apatites. Finally, though the spectra do not evidence the presence of a shoulder around 534 550 cm^{-1} the presence of apatitic HPO_4^{2-} groups in the apatite powders synthesized at 60 °C or 90 °C cannot be confirmed by FTIR because its main vibration mode $\nu_{P\,O}$ at 870 cm^{-1} coincides with the band ν_2 CO_3 at 870 cm^{-1} [58].

The carbonate content (Table 4) was determined by calculating the ratio $r_{c/p}$ between the integrated intensity of ν_3 CO_3 (1550 1350 cm^{-1} domain) and that of $\nu_1\nu_3$ PO_4 (1230 912 cm^{-1} domain) using a cali bration curve according to Grunenwald et al. method [40]. The total

Table 3
Characteristic wavenumbers of vibrations modes ν_2 CO_3 and ν_3 CO_3.

Band	*CO_3 in A-site*	*CO_3 in B-site*	*Labile CO_3*
References	[55,53]	[13,53,55,56]	[53,57]
ν_2 CO_3	878 cm ^{1}	872 cm ^{1}	866 cm ^{1}
ν_3 CO_3	1465 cm ^{1}	1412 cm ^{1}	1417 cm ^{1}
	1542 cm ^{1}	1462 cm ^{1}	1480 cm ^{1}

Table 4
Chemical composition of synthesized powders.

Powder synthesis temperature	*CO_3 wt.% (FTIR)*	*CO_3 wt.% (elemental analysis)*	*Molar ratio Ca/P (ICP/OES)*
37 °C	3.1 wt.%	3.1 wt.%	1.45 ± 0.04
60 °C	3.6 wt.%	3.5 wt.%	1.55 ± 0.08
90 °C	1.9 wt.%	1.9 wt.%	1.62 ± 0.10

carbonate content was found to be around 3 wt% with a significant decrease when the synthesis temperature is high (90 °C) in accordance with previous studies [21,22,59]. The results obtained from this spec troscopic method were in excellent agreement with carbon elemental analyses. Consequently carbonate quantification on SPS samples will be evaluated from FTIR data using the Grunenwald et al. method. Indeed, the measurement of carbonate from carbon elemental analysis could be biased by the presence of residual carbon at the sample surface re sulting from Papyex® used during SPS.

The Ca/P molar ratio determined from ICP/EOS titrations of cal cium and phosphorus was found to be lower than 1.667 (i.e. 10/6 the value of stoichiometric HA) for the three powders. It increased with the synthesis temperature (Table 4). These results are usually encountered during the synthesis of calcium deficient hydroxyapatite because of partial substitution of HPO_4^{2-} for phosphates in the apatite lattice [51]. In addition, in the present study, the samples were carbonated. A type carbonates have no effect on Ca/P ratio, but for B type carbonates the stoichiometry is defined by $Ca/(P + C_B) = 10/6$. Thus, in the presence of B type carbonation, the Ca/P ratio of powders must be greater than 10/6. Since the Ca/P values were all smaller than 1.667, the synthesized powders are clearly nonstoichiometric and must in clude other ionic species such as HPO_4^{2-} as hypothesized above.

Finally, the powder precipitated at 37 °C is an amorphous carbonate calcium phosphate whose stoichiometry is close to amorphous tri calcium phosphate composed of Posner's clusters. Its approximate for mula would be $Ca_{9-x-y}(PO_4)_{6-2x-2y}(HPO_4)_{2x}(CO_3)_{2y}{,}nH_2O$, the water is hypothesized to be in the interstices between the clusters [60].

At 60 °C a low crystalline calcium deficient carbonated apatite powder is obtained with an apatitic core approaching the chemical formula $Ca_{10-x-y}(PO_4)_{6-x-y}(HPO_4)_x(CO_3)_y(OH)_{2-x-y}$, neglecting the light carbonation in A site. These particles present also a hydrated surface layer containing labile ions (Ca^{2+}, PO_4^{3-}, HPO_4^{2-}, CO_3^{2-}, OH^-,…). The powder synthesized at 90 °C is much less hydrated and carbonated, with a higher crystallinity. Its chemical formula can be hypothesized to be $Ca_{10-x-y}(PO_4)_{6-x-y}(HPO_4)_x(CO_3)_y(OH)_{2-x-y}$ neglecting the light carbo nation in A site and the presence of a hydrated surface layer.

3.2. Spark plasma sintering

3.2.1. Influence of powder properties

The powders were heat treated by spark plasma sintering. Four distinct domains were highlighted (Fig. 5). In the first one, the regis tered increase of relative density, associated with sample shrinkage, is due to the application of the mechanical load and the associated re organization and compaction of the powder bed. The second domain corresponds to the temperature dwell at 50 °C (see Fig. 1) performed in order to homogenize the temperature in the enclosure of the SPS de vice. There is almost no change registered in this domain. In the third domain of heating from 50 °C up to 150 °C, there is no significant change for the powders synthesized at 90 °C and 60 °C. However, re garding the powder synthesized at 37 °C, a significant shrinkage of about 20% is registered at about 130 °C. Then, in the last domain, which corresponds to the dwell at 150 °C, the three compositions be have similarly with a light shrinkage of about 3 5%.

The apparent bulk density (Archimede method), solid density (pycnometry) and the final densification ratio of SPS samples are given

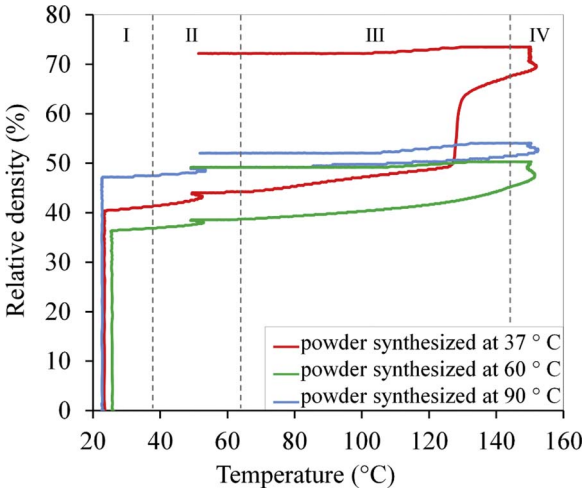

Fig. 5. Relative density changes of samples during SPS.

Table 5
Bluk density of ceramic pellets obtained after SPS.

Powder synthesis temperature	*Apparent density (g cm ^{3})*	*Solid density (g cm ^{3})*	*Densification ratio (%)*
37 °C	2.11 ± 0.02	2.973 ± 0.005	71.0
60 °C	1.49 ± 0.02	2.926 ± 0.005	49.2
90 °C	1.51 ± 0.02	2.911 ± 0.005	52.0

in Table 5. After SPS, the ceramics sintered from powders initially synthesized at 60 °C and 90 °C exhibit a quite similar densification with a final relative density of 49% and 52% of the maximum value, re spectively. This behavior is similar to that observed by Grossin et al. during the SPS of uncarbonated biomimetic nanocrystalline apatites matured 1 day [34].

XRD patterns of SPS samples are given in Fig. 6. The lattice para meters, average crystallite size and lattice distortion g_{hkl} were refined from the XRD patterns. Results are summarized in Table 6. The XRD pattern of the ceramic produced from the powder synthesized at 90 °C remains unchanged (Figs. 6 and 2). Microscopic (Fig. 7) and visual observations of the sample confirm that it did not consolidate during SPS. Grains are still rod shaped with an average size of crystallites of about 48 nm long and 28 nm width (Table 6) without change compared to the initial powder (Table 1). The crystallites just seem to have coa lesced to form grains of about 100 nm long without significant cohesion between them and the final compact remains very friable. The ceramic obtained from the powder synthesized at 60 °C also shows a

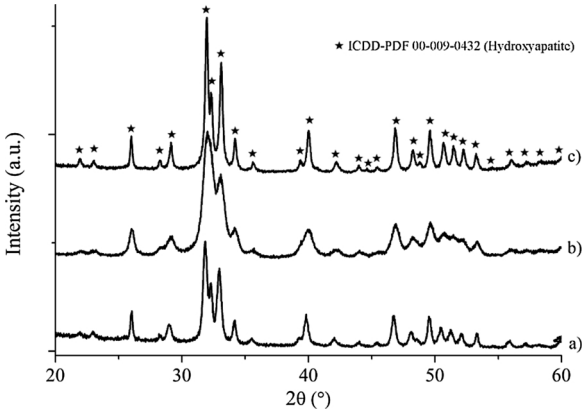

Fig. 6. XRD patterns of ceramics after SPS at 150 °C. Powder synthesized at: a) 37 °C, b) 60 °C and c) 90 °C.

Table 6
Crystallographic characteristics of SPS ceramics obtained by XRD peak fitting and carbonate content evaluated by FTIR quantification according to Grunenwald et al. method [40].

Powder synthesis temperature	*37 °C*	*60 °C*	*90 °C*
a lattice parameter (Å)	9.45(9)	9.42(6)	9.42(5)
c lattice parameter (Å)	6.88(7)	6.89(1)	6.90(1)
$L_{(310)}$ (Å)	161	74	275
$L_{(002)}$ (Å)	326	165	477
g_{hkl} (Å rad)	0.0065	0.0073	0.0057
CO_3 wt.% (FTIR)	1.5 wt.%	3.2 wt.%	1.5 wt.%

microstructure without significant changes of grain shape and size after SPS, with crystallites of about 7 nm width and 16 nm length (Fig. 7, Tables 6 and 1). Some grain boundaries can be observed suggesting that the sample sintered slightly. Nevertheless, the final ceramic remains also friable and has a low cohesion. XRD pattern shows sharper peaks after SPS than for the initial powder (Figs. 6 and 2). As the crystallite size remained unchanged this indicates a crystallinity increase of the apatite during SPS.

The powder synthesized at 37 °C shows a much higher densification, the value reaching about 71% of the maximum density after SPS (Table 5). SEM observation of the ceramic (Fig. 7) points out a densified and cohesive material with some microporosity (27.8% measured by the Archimedes' method). Biaxial flexural strength of SPS samples synthesized at 37 °C (using 5 replicates) is 18.3 ± 5 MPa. This result points out that consolidation and sintering are effective during SPS. A change of grain morphology is also noticed: from the large spherical particles of the initial powder (Fig. 2), a ceramic made of small needle like grains (Fig. 7) with crystallite size of about 33 nm length and 16 nm width (Table 6) is obtained. The observations also show that the acicular grains have grown preferentially in a plane perpendicular to the direction of the applied load during SPS. XRD pattern (Fig. 6) of the sintered ceramic reveals that the low temperature SPS of the amorphous powder leads to a crystallized apatitic phase. Thus, consolidation during SPS was accompanied by crystallization of the amorphous powder. The *a* lattice parameter is greater than that of ceramics sintered from powders synthesized at 60 °C and 90 °C. According to the literature [44,45], this expansion could be caused by insertion of CO_3^{2-} in A sites or by the presence of HPO_4^{2-} in B sites of the apatite.

FTIR spectra are given in Fig. 8. For all the ceramics the typical bands of an apatitic material are found with the vibration modes of phosphate groups (ν_1, ν_2, ν_3 and ν_4) and OH groups (ν_L and ν_S) appearing at the wavenumbers detailed in subsection 3.1. Moreover, the shoulder on the ν_4 PO_4 vibration band at 534 550 cm^{-1} attests the presence of hydrogenphosphate in the sample synthesized at 37 °C (arrow on Fig. 8b). The presence of ν_2 CO_3 and ν_3 CO_3 bands attests that carbonates are not eliminated during SPS.

Fig. 8c and d details ν_2 CO_3 and ν_3 CO_3 vibration bands and Table 6 reports the overall carbonate content estimated from FTIR spectra using the method of Grunenwald et al. [40]. The FTIR spectra of pellets obtained after SPS of powders synthesized at 90 °C or 60 °C do not show any significant change from those of the initial powders (Figs. 8 and 4).

However, a slight decrease in carbonate content is noted (Tables 6 and 4), indicating that part of the carbonate ions have decomposed and evolved as CO_2 gas during SPS, via the possible following reactions:

$$2HPO_4^{2-} + CO_3^{2-} \rightarrow 2PO_4^{3-} + H_2O + CO_2 \longrightarrow \quad (3)$$

or

$$H_2O + CO_3^{2-} \rightarrow 2OH^- + CO_2 \longrightarrow \quad (4)$$

For the amorphous powder a change of carbonate location and overall content after SPS is observed. The estimation of carbonate content by FTIR reveals a loss of half the initial carbonates during the SPS treatment. The profile of vibration bands shows the presence of carbonates in both A and B sites of the apatite as well as labile carbonates.

Because the powder synthesized at 60 °C and 90 °C did not allow the production of cohesive ceramics by SPS at low temperature (150 °C), the following subsection 3.2.2. focuses on the behavior of the amorphous carbonated calcium phosphate powder synthesized at 37 °C.

3.2.2. Thermal behavior of amorphous calcium phosphate synthesized at 37 °C

The shrinkage (fast increase of relative density) observed for carbonated ACP at about 130 °C during SPS is likely due to a concomitant consolidation and crystallization. In order to determine more precisely the behavior of this powder, other sintering conditions, including pressureless SPS, hot pressing and natural sintering were investigated. The chemical changes occurring during SPS were also analyzed.

3.2.2.1. Other sintering methods. At first, the powder was heat treated to investigate its natural sintering ability without mechanical load and pulsed electric current. DTA performed under argon flow shows an exothermic reaction starting at 630 °C with a maximum at 640 °C (Fig. 9).

In situ temperature programmed XRD was performed in a furnace under N_2 flow. Fig. 10 gives the typical diffractograms obtained from this experiment. The diffractograms registered up to 580 °C show an amorphous material whereas the pattern obtained at 620 °C exhibits a crystallized compound. Thus, the exothermic phenomenon registered by DTA is assignable to a crystallization event. The crystallized phase corresponds to beta tricalcium phosphate β TCP (ICCD 55 898) with traces of apatitic phase. This result is in accordance with the literature indicating that ACP expresses an exothermic crystallization at about 600 700 °C into β TCP [61]. But, it differs from the apatite phase obtained after SPS at 150 °C. The stabilization of apatitic phase at low temperature is linked to the structural configuration of ACP clusters. Indeed, as reported in previous works, some calcium orthophosphates including hydroxyapatite present locally the ionic arrangement of Posner's cluster [62]. This probably helps to stabilize the apatitic phase at very low temperature. Moreover, this phase transformation into apatite is similar to that observed when ACP evolves in aqueous medium leading to calcium deficient apatite [63 65].

Dilatometry (TMA) under argon flow was also performed on this material. The dilatometric curve (Fig. 11) indicates that the

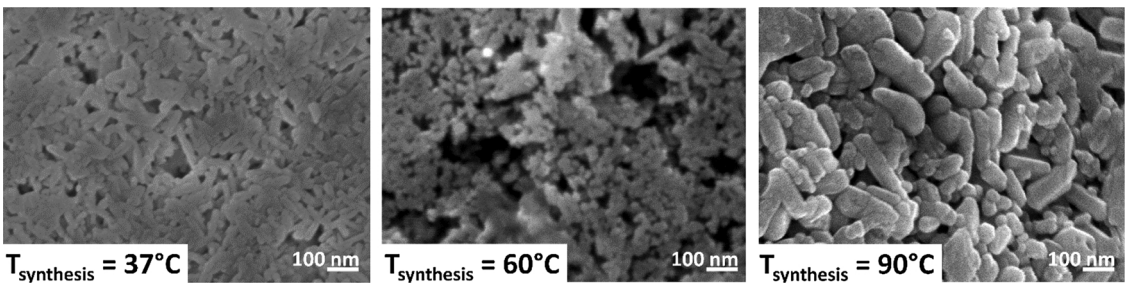

Fig. 7. SEM of ceramics surface after SPS of powders synthesized at different temperatures (observation of the surface perpendicular to the direction of the applied load).

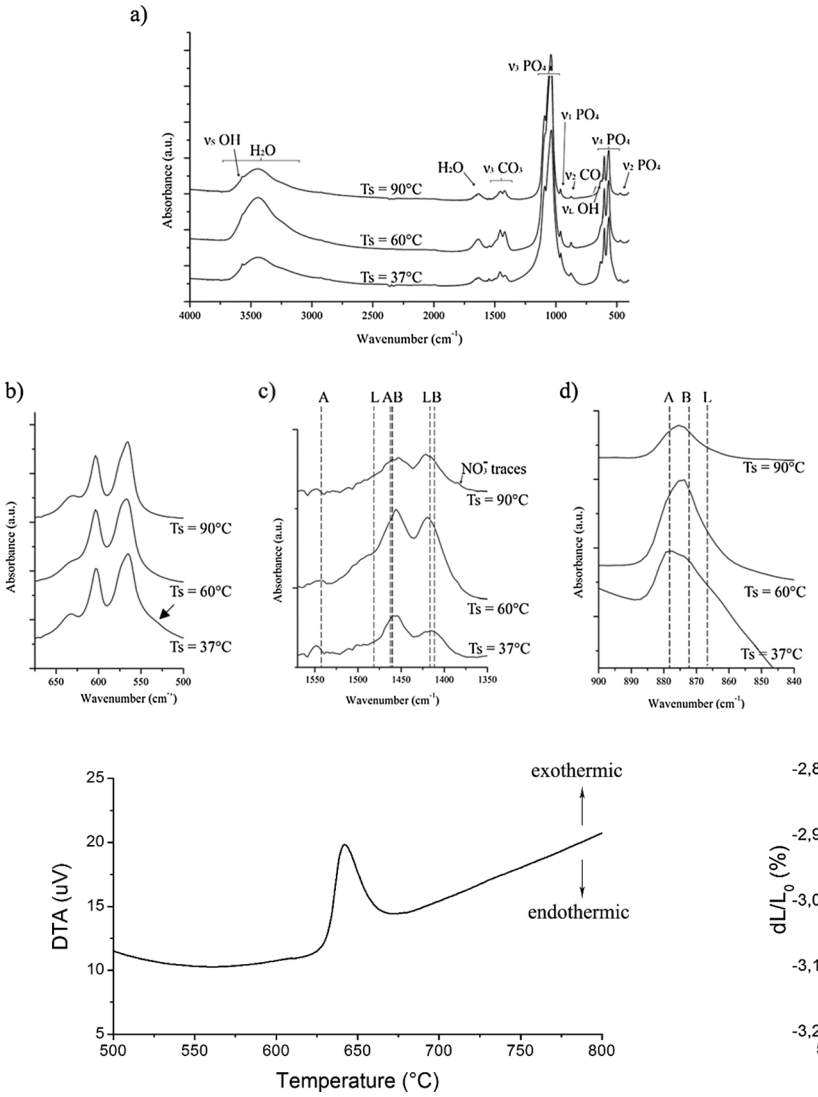

Fig. 8. FTIR spectra of SPS pellets: a) general spectra from 4000 cm ^{1} to 400 cm ^{1}, b) zoom on the ν_4 PO_4 band, c) zoom on the ν_3 CO_3 band, d) zoom on the ν_2 CO_3 band. Contributions are denoted A for A-site, B for B-site and L for labile carbonate. (Ts = Temperature of powder synthesis).

Fig. 9. DTA under argon flow of amorphous carbonated calcium phosphate powder synthesized at 37 °C.

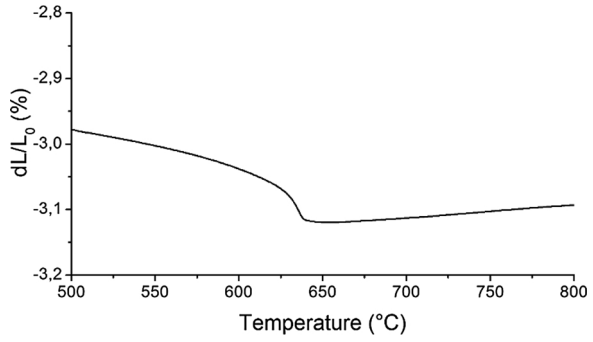

Fig. 11. TMA under argon flow of amorphous carbonated calcium phosphate powder synthesized at 37 °C.

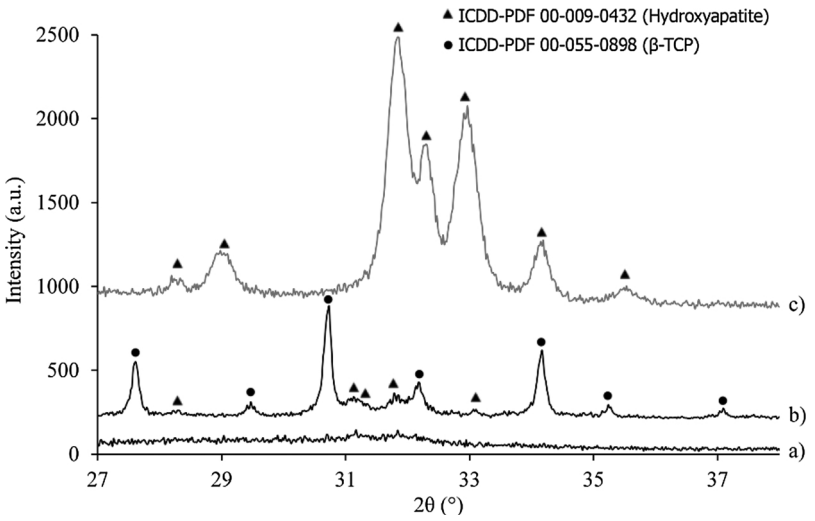

Fig. 10. Temperature programmed XRD patterns performed under N_2 flow at: a) 580 °C and b) 620 °C. c) XRD pattern at ambient temperature of sample after SPS at 150 °C. (The diffraction peaks are shifted toward low angles for diagram (b) due to the thermal expansion of the powder and sample holder).

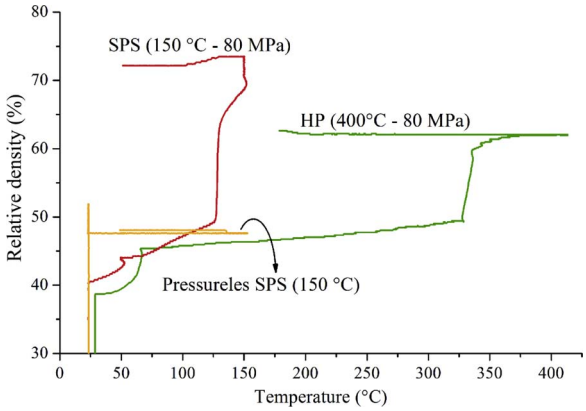

Fig. 12. Relative density changes during SPS (at 150 °C under 80 MPa), HP (at 400 °C under 80 MPa) and SPS (at 150 °C) of samples synthesized at 37 °C.

crystallization at high temperature (in the temperature range around 600 °C) is accompanied by a very light compaction (< 0.2%) in comparison with the shrinkage obtained by SPS (densification > 10% at 130 °C). Thus, crystallization that induces an increase of bulk density is not the main phenomenon responsible for the consolidation and shrinkage of carbonated apatite by SPS.

Finally, it appears that the apatitic material produced by SPS is impossible to produce by a conventional sintering method.

Complementary pressureless SPS and HP of the powder synthesized at 37 °C were carried out in order to evidence the individual contributions of an applied pressure or electric current on the sample densification. The densification curves are given in Fig. 12 in comparison with the curve of the sample densified by SPS at 150 °C under 80 MPa. During HP a shrinkage phenomenon (fast increase of relative density) similar to that observed during SPS appears but at a much higher temperature around 325 °C. Moreover, the final relative density of the HP ceramic is only 63% whereas it was 71% after SPS. Pressureless SPS only leads to a very light densification with a final relative density of 48%. The shrinkage curve is similar to that registered during SPS (under 80 MPa) of the powder synthesized at 60 °C (Fig. 5). These results highlight that the sole application of an electric current or of a mechanical load are not sufficient. Combination of both appears mandatory to provide enough activation energy for an effective densification of the material at very low temperature.

In order to complete this study, the effect of applied pressure during SPS was investigated. Assays were carried out at 175 °C under 60 MPa, 80 MPa, 100 MPa and 120 MPa. The shrinkage curves (Fig. 13) point out that the densification event shifts to higher temperature with decreasing applied load (145 °C at 60 MPa vs. 133 °C at 120 MPa). The

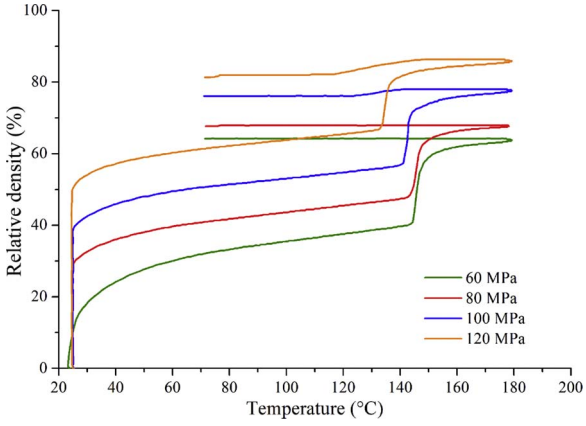

Fig. 13. Relative density changes of amorphous powder during SPS performed under different applied loads.

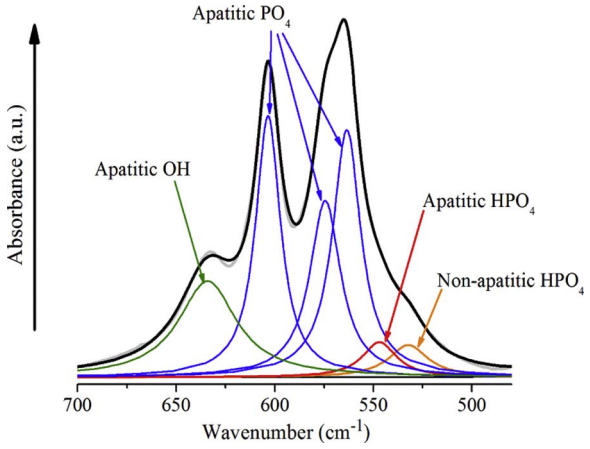

Fig. 14. Decomposition of the FTIR ν_4 PO_4 vibration region for the carbonated amorphous calcium phosphate powder after SPS at 150 °C.

supplementary mechanical energy provided by the load allows the activation of the consolidation. It must be emphasized that the difference observed between the densification curve performed at 80 MPa in this assay and the curve presented in previous subsection for the same pressure (3.2.1 Fig. 5) may be explained by the changes of the sintering cycles (see Fig. 1).

3.2.2.2. Chemical analysis of SPS ceramics. Composition changes of the material during SPS (150 °C 80 MPa) were investigated by FTIR spectroscopy. The carbonate content in the pellet was estimated according to Grunenwald's method [40]. The overall amount of CO_3^{2-} ions is 1.5 wt.%, i.e. twice less than in the initial powder (3.1 wt.%). A fraction of carbonates should have evolved as carbon dioxide gas during the treatment. The hypotheses mentioned above can be proposed to explain this loss of CO_3^{2-} (Eqs. (3) et (4)). The presence of HPO_4^{2-} ions, observed in the FTIR spectrum (arrow on Fig. 8b) and involved as reactants in Eq. (3), can be explained by an internal hydrolysis of PO_4^{3-} ions during heating after Eq. (5):

$$PO_4^{3-} + H_2O \rightarrow HPO_4^{2-} + OH^- \quad (5)$$

In order to investigate the composition of the material, a thorough study was conducted on ν_4 PO_4 and ν_2 CO_3 vibration bands. A spectral decomposition (curve fitting) to assess the area and relative intensity of the bands constituting the spectra was performed. The decomposition of ν_4 PO_4 (Fig. 14) used the wavelength position of the various contributions in accordance with previous studies on nanocrystalline apatites [45,65]. This decomposition reveals the presence of apatitic hydroxide ions. Because ACPs do not theoretically contain apatitic OH^-, such hydroxide ions should appear during the consolidation/crystallization step according to the hydrolysis of phosphates and/or carbonates (Eqs. (4) and (5), respectively). The spectral decomposition also allows highlighting the various contributions of phosphates including two kinds of HPO_4^{2-} ions: an apatitic contribution of HPO_4^{2-} located in B sites and a non apatitic contribution. A fraction of these ions, mostly in non apatitic environments, could be formed during the internal hydrolysis of phosphates (Eq. (3)). This hydrolysis reaction had already been assumed to occur in the hydrated layer during the low temperature sintering of nanocrystalline apatites by Drouet et al. [35]. These observations tend to confirm our first hypothesis: decarbonation observed during SPS would be mainly caused by an internal hydrolysis of the PO_4^{3-} groups (Eq. (5)) followed by the decomposition of the carbonates by reaction with the non apatitic HPO_4^{2-} (Eq. (3)) rather than a direct hydrolysis of carbonates (Eq. (4)).

In order to identify and quantify the proportions of the different kinds of carbonates in the SPS ceramic, the ν_2 CO_3 spectrum in the region 840 900 cm^{-1} was also decomposed. HPO_4^{2-} and CO_3^{2-} ions

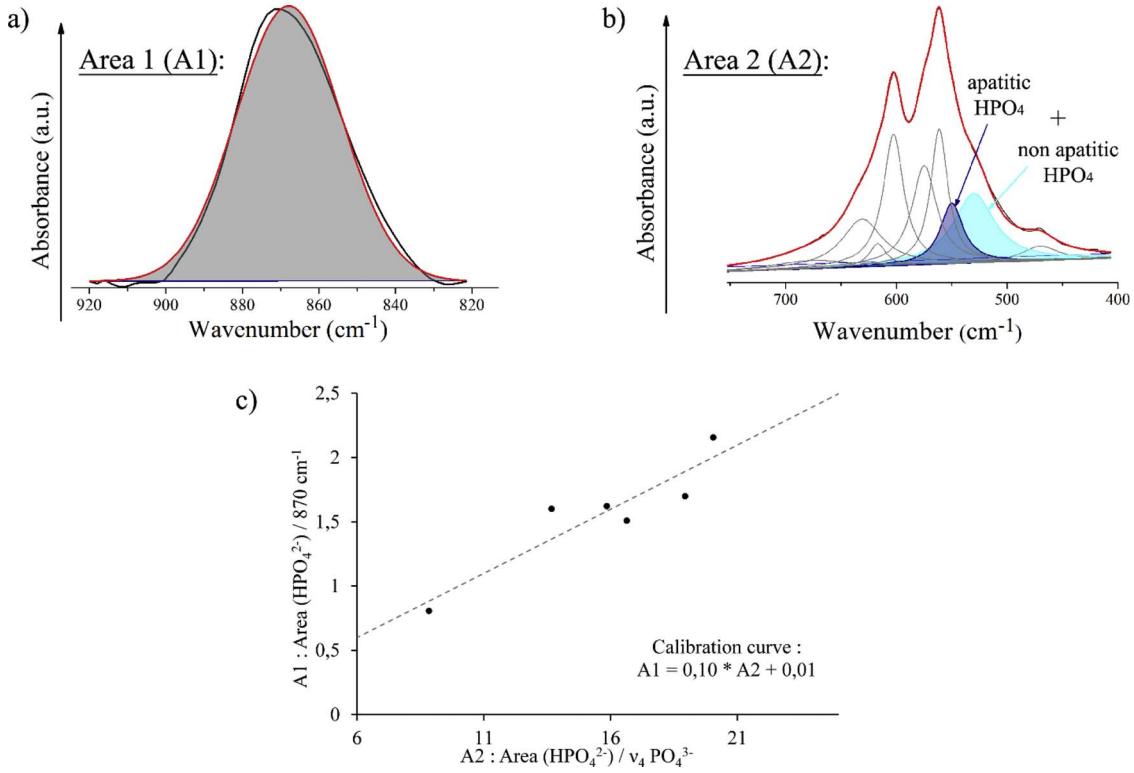

Fig. 15. HPO_4^{2} ions area (A1) at 870 cm ^{1} (a) and areas (A2) in the ν_4PO_4 region (b), calibration curve relating these areas (c).

exhibit vibrations at similar wavenumbers around 870 cm^{-1} which makes it difficult to isolate the respective contributions of these ionic groups. To overcome this difficulty, a preliminary study was carried out using uncarbonated nanocrystalline apatite powders containing various amounts of HPO_4^{2-} ions. This allowed to relate the area of HPO_4^{2-} bands in the domain of ν_4 PO_4 band (Fig. 15b) to the area of the as sociated band at 870 cm^{-1} (Fig. 15a). Powders were synthesized by aqueous precipitation following a rapid addition of a solution of cal cium nitrate to a solution of ammonium hydrogen phosphate. The precipitates were matured for various times, resulting in varying amounts of hydrogenphosphate ions in the powder. Then, the decom position of the FTIR bands according to the method proposed by Van decandelaere et al. [45] was performed. The calibration curve (Fig. 15c) obtained after calculation of the areas of hydrogen phosphate vibration bands gives the coefficient that relates the sum of HPO_4^{2-} bands areas (A2) in the ν_4 PO_4 region to the area (A1) of the associated band at 870 cm^{-1}. This calibration curve was used to calculate the area (A1) of the HPO_4^{2-} band at 870 cm^{-1} in the domain of ν_2 CO_3 bands (Fig. 15) from the area (A2) of the HPO_4^{2-} bands in the domain of ν_4 PO_4 band of the SPS sample (Fig. 14).

Carbonate contributions were positioned at the wavenumbers given in Table 3 to decompose the ν_2 CO_3 bands. The carbonate species contained in the amorphous powder before SPS are hypothesized in a labile position. After SPS (Fig. 16), 28.6% of the remaining carbonates are labile and three quarters of the total amount have migrated in the A and B sites of the formed apatite with 27.8% and 43.6% respectively.

This decomposition highlights also the presence of non apatitic ions in the sintered ceramic, as the spectrum decomposition reveals the presence of some labile carbonates but also of non apatitic HPO_4^{2-} ions. Thus, it can be stated that the material obtained after SPS is si milar to biomimetic nanocrystalline apatites [31], composed of non stoichiometric crystalline carbonated apatitic grains ($Ca_{10-x-y}(PO_4)_{6-x-y}(HPO_4)_x(CO_3)_y(OH)_{2-x-y-2z}(CO_3)_z$) surrounded by a non apatitic hy drated layer which constitutes the grain boundaries as denoted in the

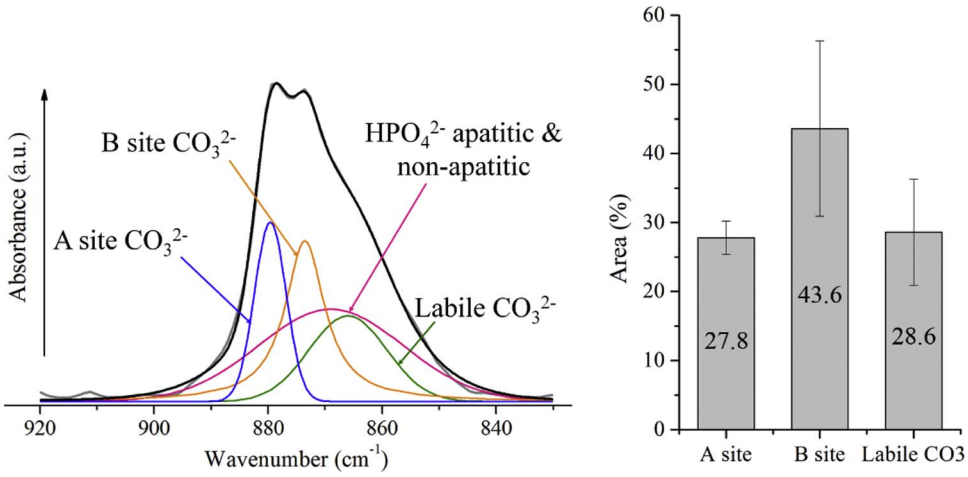

Fig. 16. Decomposition of ν_2 CO_3 band and ratios of carbonate band areas after SPS at 150 °C of the amorphous calcium carbonate powder synthesized at 37 °C.

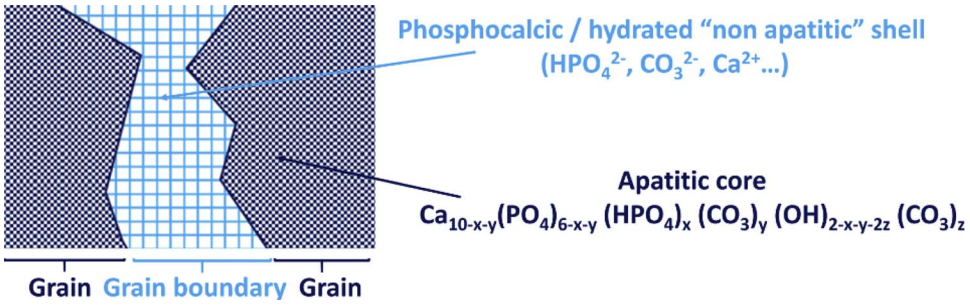

Fig. 17. Schematic representation of the SPS ceramic.

schematic representation of the resulting ceramic (Fig. 17).

3.2.3. Discussion

It was pointed out by Grossin et al. in the case of non carbonated nanocrystalline apatite sintered at low temperature by SPS that the classical mechanisms of diffusion and grain growth occurring during conventional sintering at high temperature cannot happen below 300 °C [34]. Classical solid state diffusion in crystallized compounds cannot be activated at such low temperatures. The authors stated the importance of the presence of a hydrated layer surrounding the apatitic core of nanoparticles which was characterized by a high ionic mobility. This statement is confirmed in our study since the powders synthesized at 60 °C and 90 °C which are crystallized and have a very small or an absence of hydrated surface layer could not consolidate by low temperature SPS at 150 °C. Amorphous calcium phosphate powders can be assimilated to fully non apatitic hydrated phosphocalcic grains (the clusters being surrounded by 15 20% of residual water in the interstices of the Posner structure). This implies high solid state ion mobility at very low temperature favoring chemical reactions and leading to the formation of grains (apatitic core) that crystallize into an apatitic structure and grow preferentially along their c axis, while the surrounding hydrated layers of adjacent grains fuse to form the grain boundaries. This results in high strength porous ceramics. Such a sintering, recalling the mechanisms involved in cold sintering of ferroelectric materials [66,67], processes through a phenomenon previously called "crystal fusion" enhanced by the additional activation energy provided by an applied load [34,35]. In our case, calcium deficient carbonated apatite of chemical composition $Ca_{10-x-z}(PO_4)_{6-x-z}(HPO_4)_x(CO_3)_z(OH)_{2-x-2y-z}(CO_3)_y$ crystalizes from the amorphous clusters that formed the initial spherical grains leading to nanometric acicular grains after SPS. Starting from an amorphous powder was found to be necessary in carbonated systems to enhance the densification and provide a chemical composition very close to that of the mineral part of bone. This contrasts with the conventional sintering of calcium deficient apatites that leads to mixtures of well crystallized stoichiometric calcium phosphates ($Ca_2P_2O_7$ + TCP, TCP or HA + TCP) from about 700 °C [68].

Although the mechanism involved in this process remains to be analyzed in more detail, it can be stated that the methods described previously in the literature, starting from crystalized powders, are unlikely to achieve in the production of highly cohesive bioceramics of chemical composition and structure very close to the mineral phase of bone. Such "bone like" ceramics are expected to provide superior biological properties, the evaluation of which is under consideration.

4. Conclusion

Carbonated calcium phosphate powders of various composition and crystallinity level were synthesized by aqueous precipitation at different temperatures. These powders were heat treated by Spark Plasma Sintering at very low temperature (150 °C). Only the amorphous carbonated calcium phosphate powder, precipitated at the physiologic temperature of 37 °C, could be sintered at such a low temperature. The consolidation is accompanied with crystallization of the amorphous phase into carbonated apatite. The high flexural strength of the resulting microporous ceramic confirms the efficiency of Spark Plasma Sintering. This ceramic is made of a low crystalline nonstoichiometric carbonated apatite. The grains are composed of an apatitic core surrounded by a hydrated layer containing non apatitic ions which constitutes the grain boundaries. The high mobility of chemical species of the initially amorphous powder appears responsible for the consolidation of the sample at low temperature by surface ionic diffusion process enhanced by the applied load and electrical current during SPS. This leads to the formation of non apatitic grain boundaries while the core of grains crystallizes. It can be emphasized that the SPS of amorphous calcium phosphates makes it possible to consolidate a calcium deficient carbonated apatitic phase of generic composition $Ca_{10-x-z}(PO_4)_{6-x-z}(HPO_4)_x(CO_3)_z(OH)_{2-x-2y-z}(CO_3)_y$ which is impossible to preserve by conventional sintering.

Acknowledgements

C. Ortali thanks to the French "Conseil Régional du Limousin" for her PhD funding and the Groupe Français de la Céramique (GFC) for financial support of internship at the CIRIMAT Laboratory. This work is supported at SPCTS by institutional grants from the LabEX SigmaLim (ANR 10 LABX 0074 01).

References

[1] S.V. Dorozhkin, Nanosized and nanocrystalline calcium orthophosphates, Acta Biomater. 6 (2010) 715–734, http://dx.doi.org/10.1016/j.actbio.2009.10.031.

[2] J.A. Juhasz, S.M. Best, Bioactive ceramics: processing, structures and properties, J. Mater. Sci. 47 (2012) 610–624, http://dx.doi.org/10.1007/s10853-011-6063-x.

[3] Chapter 1 – general chemistry of the calcium orthophosphates, in: J.C. Elliott (Ed.), Stud. Inorg. Chem. Elsevier, 1994, pp. 1–62 http://www.sciencedirect.com/science/article/pii/B9780444815828500067 (Accessed 16 October 2016).

[4] J.H. Shepherd, D.V. Shepherd, S.M. Best, Substituted hydroxyapatites for bone repair, J. Mater. Sci. Mater. Med. 23 (2012) 2335–2347, http://dx.doi.org/10.1007/s10856-012-4598-2.

[5] R. Legros, N. Balmain, G. Bonel, Structure and composition of the mineral phase of periosteal bone, J. Chem. Res. Synop. (1986) 8–9.

[6] J.C. Elliott, D.W. Holcomb, R.A. Young, Infrared determination of the degree of substitution of hydroxyl by carbonate ions in human dental enamel, Calcif. Tissue Int. 37 (1985) 372–375, http://dx.doi.org/10.1007/BF02553704.

[7] M. Vallet-Regi, J. Gonzales-Calbet, Calcium phosphates as substitution of bone tissues, Prog. Solid State Chem. 32 (2004) 1–31, http://dx.doi.org/10.1016/j.progsolidstchem.2004.07.001.

[8] J.C. Trombe, G. Montel, Some features of the incorporation of oxygen in different oxidation states in the apatitic lattice—I On the existence of calcium and strontium oxyapatites, J. Inorg. Nucl. Chem. 40 (1978) 15–21, http://dx.doi.org/10.1016/0022-1902(78)80298-X.

[9] G. Penel, G. Leroy, C. Rey, E. Bres, MicroRaman spectral study of the PO4 and CO3 vibrational modes in synthetic and biological apatites, Calcif. Tissue Int. 63 (1998) 475–481, http://dx.doi.org/10.1007/s002239900561.

[10] I.R. Gibson, W. Bonfield, Novel synthesis and characterization of an AB-type carbonate-substituted hydroxyapatite, J. Biomed. Mater. Res. 59 (2002) 697–708, http://dx.doi.org/10.1002/jbm.10044.

[11] D. Tadic, F. Peters, M. Epple, Continuous synthesis of amorphous carbonated apatites, Biomaterials 23 (2002) 2553–2559, http://dx.doi.org/10.1016/S0142-9612(01)00390-8.

[12] R.Z. LeGeros, O.R. Trautz, E. Klein, J.P. LeGeros, Two types of carbonate substitution in the apatite structure, Experientia 25 (1968) 5–7, http://dx.doi.org/10.1007/BF01903856.

[13] Chapter 4 – mineral, synthetic and biological carbonate apatites, in: J.C. Elliott (Ed.), Stud. Inorg. Chem. Elsevier, 1994, pp. 191–304 http://www.sciencedirect.

com/science/article/pii/B9780444815828500092 (Accessed 16 October 2016).
[14] J.P. Lafon, E. Champion, D. Bernache-Assollant, Processing of AB-type carbonated hydroxyapatite Ca10-x(PO4)6-x(CO3)x(OH)2-x-2y(CO3)y ceramics with controlled composition, J. Eur. Ceram. Soc. 28 (2008) 139–147, http://dx.doi.org/10.1016/j.jeurceramsoc.2007.06.009.
[15] Y. Doi, T. Shibutani, Y. Moriwaki, T. Kajimoto, Y. Iwayama, Sintered carbonate apatites as bioresorbable bone substitutes, J. Biomed. Mater. Res. 39 (1998) 603–610, http://dx.doi.org/10.1002/(SICI)1097-4636(19980315)39:4<603:AID-JBM15>3.0.CO;2-7.
[16] L.T. Bang, B.D. Long, R. Othman, Carbonate hydroxyapatite and silicon-substituted carbonate hydroxyapatite: synthesis, mechanical properties, and solubility evaluations, Sci. World J. 2014 (2014) e969876, http://dx.doi.org/10.1155/2014/969876.
[17] Y. Deng, Y. Sun, X. Chen, P. Zhu, S. Wei, Biomimetic synthesis and biocompatibility evaluation of carbonated apatites template-mediated by heparin, Mater. Sci. Eng. C 33 (2013) 2905–2913, http://dx.doi.org/10.1016/j.msec.2013.03.016.
[18] B.R. Adams, A. Mostafa, Z. Schwartz, B.D. Boyan, Osteoblast response to nanocrystalline calcium hydroxyapatite depends on carbonate content, J. Biomed. Mater. Res. A 102 (2014) 3237–3242, http://dx.doi.org/10.1002/jbm.a.34994.
[19] M.-M. Germaini, R. Detsch, A. Grünewald, A. Magnaudeix, F. Lalloué, A. Boccaccini, E. Champion, Osteoblast and osteoclast responses to A/B type carbonate-substituted hydroxyapatite ceramics for bone regeneration, Biomed. Mater. 12 (2017) 035008, , http://dx.doi.org/10.1088/1748-605X/aa69c3.
[20] Y. Doi, T. Koda, N. Wakamatsu, Influence of carbonate on sintering of apatites, J. Dent. Res. 72 (1993) 1279–1284.
[21] C. Vignoles, Contribution à l'étude de l'influence des ions alcalins sur la carbonatation dans les sites de type B des apatites phosphocalciques, Université Paul Sabatier, Toulouse, 1973.
[22] J.C. Labarthe, G. Bonel, G. Montel, Sur la structure et les proprités des apatites carbonatées de type B phospho-calciques, Ann. Chim. 8 (1973) 289–301.
[23] Z. Zyman, M. Tkachenko, CO2 gas-activated sintering of carbonated hydroxyapatites, J. Eur. Ceram. Soc. 31 (2011) 241–248, http://dx.doi.org/10.1016/j.jeurceramsoc.2010.09.005.
[24] U. Anselmi-Tamburini, S. Gennari, J.E. Garay, Z.A. Munir, Fundamental investigations on the spark plasma sintering/synthesis process: II. Modeling of current and temperature distributions, Mater. Sci. Eng. A 394 (2005) 139–148, http://dx.doi.org/10.1016/j.msea.2004.11.019.
[25] M.N. Rahaman, Ceramic Processing and Sintering, CRC Press, 2003.
[26] Y.W. Gu, N.H. Loh, K.A. Khor, S.B. Tor, P. Cheang, Spark plasma sintering of hydroxyapatite powders, Biomaterials 23 (2002) 37–43, http://dx.doi.org/10.1016/S0142-9612(01)00076-X.
[27] A. Cuccu, S. Montinaro, R. Orrù, G. Cao, D. Bellucci, A. Sola, V. Cannillo, Consolidation of different hydroxyapatite powders by SPS: optimization of the sintering conditions and characterization of the obtained bulk products, Ceram. Int. 41 (2015) 725–736, http://dx.doi.org/10.1016/j.ceramint.2014.08.131.
[28] M. Buchi Suresh, P. Biswas, V. Mahender, R. Johnson, Comparative evaluation of electrical conductivity of hydroxyapatite ceramics densified through ramp and hold, spark plasma and post sinter Hot Isostatic Pressing routes, Mater. Sci. Eng. C 70 (Part 1) (2017) 364–370, http://dx.doi.org/10.1016/j.msec.2016.09.023.
[29] S.J. Kalita, H.A. Bhatt, Nanocrystalline hydroxyapatite doped with magnesium and zinc: synthesis and characterization, Mater. Sci. Eng. C 27 (2007) 837–848, http://dx.doi.org/10.1016/j.msec.2006.09.036.
[30] S. Cazalbou, D. Eichert, X. Ranz, C. Drouet, C. Combes, M.F. Harmand, C. Rey, Ion exchanges in apatites for biomedical application, J. Mater. Sci. Mater. Med. 16 (2005) 405–409, http://dx.doi.org/10.1007/s10856-005-6979-2.
[31] D. Eichert, C. Drouet, H. Sfihi, C. Rey, C. Combes, Nanocrystalline apatite-based biomaterials: synthesis, processing and characterization, Biomater. Res. Adv. Nova Science Publishers, 2007.
[32] D. Eichert, C. Combes, C. Drouet, C. Rey, Formation and evolution of hydrated surface layers of apatites, Key Eng. Mater. 284–286 (2005) 3–6.
[33] C. Drouet, M.-T. Carayon, C. Combes, C. Rey, Surface enrichment of biomimetic apatites with biologically-active ions Mg2+ and Sr2+: a preamble to the activation of bone repair materials, Mater. Sci. Eng. C 28 (2008) 1544–1550, http://dx.doi.org/10.1016/j.msec.2008.04.011.
[34] D. Grossin, S. Rollin-Martinet, C. Estournès, F. Rossignol, E. Champion, C. Combes, C. Rey, C. Geoffroy, C. Drouet, Biomimetic apatite sintered at very low temperature by spark plasma sintering: physico-chemistry and microstructure aspects, Acta Biomater. 6 (2010) 577–585, http://dx.doi.org/10.1016/j.actbio.2009.08.021.
[35] C. Drouet, F. Bosc, M. Banu, C. Largeot, C. Combes, G. Dechambre, C. Estournès, G. Raimbeaux, C. Rey, Nanocrystalline apatites: from powders to biomaterials, Powder Technol. 190 (2009) 118–122, http://dx.doi.org/10.1016/j.powtec.2008.04.041.
[36] F. Brouillet, D. Laurencin, D. Grossin, C. Drouet, C. Estournes, G. Chevallier, C. Rey, Biomimetic apatite-based composite materials obtained by spark plasma sintering (SPS): physicochemical and mechanical characterizations, J. Mater. Sci. Mater. Med. 26 (2015) 223, http://dx.doi.org/10.1007/s10856-015-5553-9.
[37] A. Coulon, D. Laurencin, A. Grandjean, S. Le Gallet, L. Minier, S. Rossignol, L. Campayo, Key parameters for spark plasma sintering of wet-precipitated iodate-substituted hydroxyapatite, J. Eur. Ceram. Soc. 36 (2016) 2009–2016, http://dx.doi.org/10.1016/j.jeurceramsoc.2016.02.041.
[38] P. Scherrer, Bestimmung der Größe und der inneren Struktur von Kolloidteilchen mittels Röntgenstrahlen, Nachrichten Von Ges. Wiss. Zu Gött. Math.-Phys. Kl. 1918 (1918) 98–100.
[39] W. Vogel, R. Hosemann, Evaluation of paracrystalline distortions from line broadening, Acta Crystallogr. A 26 (1970) 272–277, http://dx.doi.org/10.1107/S0567739470000657.
[40] A. Grunenwald, C. Keyser, A.M. Sautereau, E. Crubézy, B. Ludes, C. Drouet, Revisiting carbonate quantification in apatite (bio)minerals: a validated FTIR methodology, J. Archaeol. Sci. 49 (2014) 134–141, http://dx.doi.org/10.1016/j.jas.2014.05.004.
[41] J.A. Meganck, M.J. Baumann, E.D. Case, L.R. McCabe, J.N. Allar, Biaxial flexure testing of calcium phosphate bioceramics for use in tissue engineering, J. Biomed. Mater. Res. A 72A (2005) 115–126, http://dx.doi.org/10.1002/jbm.a.30213.
[42] R.Z. LeGeros, Effect of carbonate on the lattice parameters of apatite, Nature 206 (1965) 403–404, http://dx.doi.org/10.1038/206403a0.
[43] E. Landi, G. Celotti, G. Logroscino, A. Tampieri, Carbonated hydroxyapatite as bone substitute, J. Eur. Ceram. Soc. 23 (2003) 2931–2937, http://dx.doi.org/10.1016/S0955-2219(03)00304-2.
[44] J.C. Elliott, Space group and lattice constants of $Ca_{10}(PO_4)_6CO_3$, J. Appl. Crystallogr. 13 (1980) 618–621, http://dx.doi.org/10.1107/S0021889880012927.
[45] N. Vandecandelaere, C. Rey, C. Drouet, Biomimetic apatite-based biomaterials: on the critical impact of synthesis and post-synthesis parameters, J. Mater. Sci. Mater. Med. 23 (2012) 2593–2606, http://dx.doi.org/10.1007/s10856-012-4719-y.
[46] A.L. Boskey, Amorphous calcium phosphate: the contention of bone, J. Dent. Res. 76 (1997) 1433–1436.
[47] S.V. Dorozhkin, Amorphous calcium (ortho)phosphates, Acta Biomater. 6 (2010) 4457–4475.
[48] F. Betts, N.C. Blumenthal, A.S. Posner, G.L. Becker, A.L. Lehninger, Atomic structure of intracellular amorphous calcium phosphate deposits, Proc. Natl. Acad. Sci. 72 (1975) 2088–2090, http://dx.doi.org/10.1073/pnas.72.6.2088.
[49] A.S. Posner, F. Betts, N.C. Blumenthal, Formation and structure of synthetic and bone hydroxyapatites, Prog. Cryst. Growth Charact. 3 (1980) 49–64, http://dx.doi.org/10.1016/0146-3535(80)90011-8.
[50] C. Holt, D.W.L. Hukins, Structural analysis of the environment of calcium ions in crystalline and amorphous calcium phosphates by X-ray absorption spectroscopy and a hypothesis concerning the biological function of the casein micelle, Int. Dairy J. 1 (1991) 151–165, http://dx.doi.org/10.1016/0958-6946(91)90008-V.
[51] S. Raynaud, E. Champion, D. Bernache-Assollant, P. Thomas, Calcium phosphate apatites with variable Ca/P atomic ratio I. Synthesis, characterisation and thermal stability of powders, Biomaterials 23 (2002) 1065–1072, http://dx.doi.org/10.1016/S0142-9612(01)00218-6.
[52] B.O. Fowler, E.C. Moreno, W.E. Brown, Infra-red spectra of hydroxyapatite, octacalcium phosphate and pyrolysed octacalcium phosphate, Arch. Oral Biol. 11 (1966) 477–492.
[53] C. Rey, C. Combes, C. Drouet, D. Grossin, Bioactive ceramics: physical chemistry, Compr. Biomater, (2011), pp. 187–221.
[54] C. Holt, M.J.J.M. Van Kemenade, L.S. Nelson, D.W.L. Hukins, R.T. Bailey, J.E. Harries, S.S. Hasnain, P.L. De Bruyn, Amorphous calcium phosphates prepared at pH 6.5 and 6.0, Mater. Res. Bull. 24 (1989) 55–62, http://dx.doi.org/10.1016/0025-5408(89)90008-1.
[55] M. Vignoles, G. Bonel, D.W. Holcomb, R.A. Young, Influence of preparation conditions on the composition of type B carbonated hydroxyapatite and on the localization of the carbonate ions, Calcif. Tissue Int. 43 (1988) 33–40, http://dx.doi.org/10.1007/BF02555165.
[56] H.E. Feki, C. Rey, M. Vignoles, Carbonate ions in apatites: infrared investigations in thev4 CO3 domain, Calcif. Tissue Int. 49 (1991) 269–274, http://dx.doi.org/10.1007/BF02556216.
[57] C. Rey, J. Lian, M. Grynpas, F. Shapiro, L. Zylberberg, M.J. Glimcher, Non-apatitic environments in bone mineral: FT-IR detection, biological properties and changes in several disease states, Connect. Tissue Res. 21 (1989) 267–273, http://dx.doi.org/10.3109/03008208909050016.
[58] Chapter 3 – hydroxyapatite and nonstoichiometric apatites, in: J.C. Elliott (Ed.), Stud. Inorg. Chem. Elsevier, 1994, pp. 111–189 http://www.sciencedirect.com/science/article/pii/B9780444815828500080 (Accessed 16 October 2016).
[59] J. Barralet, S. Best, W. Bonfield, Carbonate substitution in precipitated hydroxyapatite: an investigation into the effects of reaction temperature and bicarbonate ion concentration, J. Biomed. Mater. Res. 41 (1998) 79–86, http://dx.doi.org/10.1002/(SICI)1097-4636(199807)41:1<79:AID-JBM10>3.0.CO;2-C.
[60] J.-C. Heughebaert, Contribution à l'étude de l'évolution des orthophosphates de calcium précipités amorphes en orthophosphates apatitiques, Institut National Polytechnique de Toulouse, 1977.
[61] S.V. Dorozhkin, Amorphous calcium phosphates, J. Biomim. Biomater. Tissue Eng. 7 (2010) 27–53, http://dx.doi.org/10.4028/www.scientific.net/JBBTE.7.27.
[62] C. Combes, C. Rey, Amorphous calcium phosphates: synthesis, properties and uses in biomaterials, Acta Biomater. 6 (2010) 3362–3378, http://dx.doi.org/10.1016/j.actbio.2010.02.017.
[63] A.L. Boskey, A.S. Posner, Conversion of amorphous calcium phosphate to microcrystalline hydroxyapatite. A pH-dependent, solution-mediated, solid-solid conversion, J. Phys. Chem. 77 (1973) 2313–2317, http://dx.doi.org/10.1021/j100638a011.
[64] J.C. Heughebaert, G. Montel, Conversion of amorphous tricalcium phosphate into apatitic tricalcium phosphate, Calcif. Tissue Int. 34 (Suppl. 2) (1982) S103–S108.
[65] C. Rey, C. Combes, C. Drouet, A. Lebugle, H. Sfihi, A. Barroug, Nanocrystalline apatites in biological systems: characterisation, structure and properties, Mater. Werkst. 38 (2007) 996–1002, http://dx.doi.org/10.1002/mawe.200700229.
[66] H. Guo, A. Baker, J. Guo, C.A. Randall, Cold sintering process: a novel technique for low-temperature ceramic processing of ferroelectrics, J. Am. Ceram. Soc. 99 (2016) 3489–3507, http://dx.doi.org/10.1111/jace.14554.
[67] J. Guo, H. Guo, A.L. Baker, M.T. Lanagan, E.R. Kupp, G.L. Messing, C.A. Randall, Cold sintering: a paradigm shift for processing and integration of ceramics, Angew. Chem. Int. Ed. 55 (2016) 11457–11461, http://dx.doi.org/10.1002/anie.201605443.
[68] S. Raynaud, E. Champion, D. Bernache-Assollant, Calcium phosphate apatites with variable Ca/P atomic ratio II. Calcination and sintering, Biomaterials 23 (2002) 1073–1080, http://dx.doi.org/10.1016/S0142-9612(01)00219-8.